Chinese Chemical Letters 35 (2024) 109886

Contents lists available at ScienceDirect

Chinese Chemical Letters

journal homepage: www.elsevier.com/locate/cclet

Synergy of sodium doping and nitrogen defects in carbon nitride for promoted photocatalytic synthesis of hydrogen peroxide

Fabrice Nelly Habarugira[a,1], Ducheng Yao[a,1], Wei Miao[b], Chengcheng Chu[a], Zhong Chen[a], Shun Mao[a,*]

[a] College of Environmental Science and Engineering, State Key Laboratory of Pollution Control and Resource Reuse, Tongji University, Shanghai 200092, China
[b] Baowu Water Technology Co., Ltd. Research Institute, Shanghai 201999, China

ARTICLE INFO

Article history:
Received 30 December 2023
Revised 21 February 2024
Accepted 11 April 2024
Available online 12 April 2024

Keywords:
Photocatalysis
H_2O_2 evolution
Sodium doping
Nitrogen defect
Metal-free catalyst

ABSTRACT

Photocatalytic synthesis of hydrogen peroxide has gradually become a promising method for *in-situ* production of hydrogen peroxide, which relies on sustainable solar energy. However, the commonly used photocatalyst, *i.e.*, carbon nitride (CN), still suffers from the drawbacks of narrow light absorption range and fast charge recombination. Here, we report a facile method to introduce nitrogen defects into carbon nitride together with sodium ion. By adjusting the ratio of sodium dicyandiamide, the band gap of carbon nitride can be controlled, while the carrier separation and transfer ability of carbon nitride is improved. The modified CN with sodium doping and nitrogen defect (SD-CN) demonstrates outstanding H_2O_2 production performance (H_2O_2 yield rate of 297.2 μmol L^{-1} h^{-1}) under visible light irradiation, which is approximately 9.8 times higher than that of pristine CN. This work deepens the understanding of the coordinated effect of structural defect and element doping of carbon nitride on the photocatalytic H_2O_2 production performance, and provides new insight into the design of photocatalytic system for efficient production of H_2O_2.

Hydrogen peroxide (H_2O_2) is one of the most useful chemicals in the pharmaceutical, chemical and food industries as well as in environmental management [1–4]. It is widely used in chemical processing, textile and pulp bleaching, waste material treatment and reaction catalysis. In addition, H_2O_2 is a potential candidate for carbonaceous fuels for power generation [5–9]. Conventional large-scale production of H_2O_2 relies on the energy-intensive anthraquinone method [10], which possesses potential flammability and explosion risk. The *in-situ* production of H_2O_2 is one of the important future development directions of sustainable synthesis of H_2O_2, which can significantly reduce H_2O_2 transportation cost and minimize safety concern [11–14]. The synthesis of hydrogen peroxide through photocatalytic process is gaining popularity due to the utilization of sunshine without the need for extra energy [15].

Over the past ten years, carbon nitride (CN) has been thoroughly studied as a metal-free polymer semiconductor material for many kinds of photocatalytic processes [16–18]. In 2014, Hirai *et al.* first demonstrated carbon nitride's enormous potential for photocatalytic H_2O_2 generation [19]. Their finding shows that the reaction forms a stable endoperoxide intermediate with 90% H_2O_2 selectivity. However, due to the restriction of rapid charge recombination, the photocatalytic activity of pristine carbon nitride for H_2O_2 generation is still unsatisfactory [20–23]. Because of this, scientists have proposed different strategies to address the issues of carbon nitride, such as creating heterojunction, adding structural flaw, and constructing nanostructured carbon nitride [24–26].

Among them, the method of introducing defects is the most common means of modification [27–30]. For instance, adding nitrogen vacancies to the carbon nitride network can speed up charge separation and improve the light trapping, resulting in the greatly promoted H_2O_2 production rate [31]. However, this modified carbon nitride is poorly stabilized and quickly deactivated after a few hours under visible light irradiation [32,33]. The light trapping and carrier separation of carbon nitride can be enhanced by alkali metal doping [34]. Pan *et al.* prepared porous ordered carbon nitride using $KHCO_3$ as a template [35], and successfully introduced K atoms and cyano into the carbon nitride skeleton structure. The K-doping adjusted the electronic structure of carbon nitride and improved the photocatalytic activity of H_2O_2 production. Although these modification strategies have been

* Corresponding author.
E-mail address: shunmao@tongji.edu.cn (S. Mao).
[1] These authors contributed equally to this work.

https://doi.org/10.1016/j.cclet.2024.109886
1001-8417/

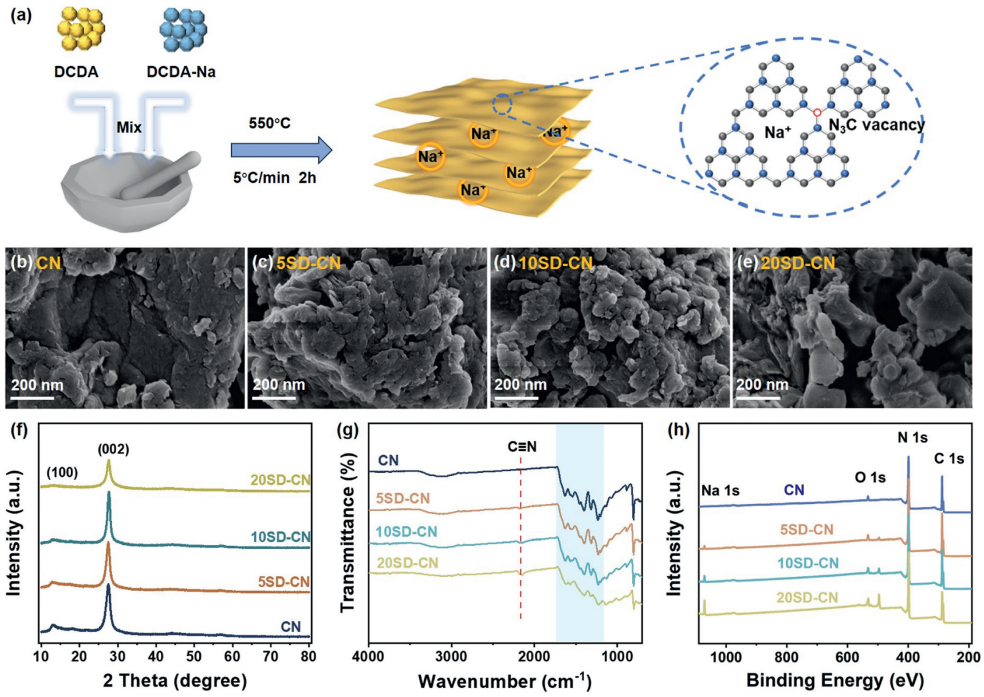

Fig. 1. (a) Schematic illustration of the preparation process of the SD-CN catalyst. SEM images of (b) CN, (c) 5SD-CN, (d) 10SD-CN, (e) 20SD-CN. (f) XRD patterns, (g) FT-IR spectra, and (h) XPS survey spectra of CN, 5SD-CN, 10SD-CN and 20SD-CN.

proved to improve the catalytic performance of carbon nitride, the overall performance of carbon nitride is still limited. The structural engineering of carbon nitride by combining two or more of these strategies could be a key to the performance breakthrough.

Herein, we report a modified carbon nitride by fusion polymerization of sodium dicyandiamide and dicyandiamide to achieve multiscale structural engineering with simultaneous introduction of nitrogen defects and alkali metal doping (Fig. 1a). By adjusting the ratio of sodium dicyandiamide during the synthesis process, the light trapping property, carrier separation performance, and charge transfer capability of the modified carbon nitride can be effectively controlled. The modified carbon nitride exhibits significantly increased photocatalytic H_2O_2 production activity, which is 9.8 higher than that of the pristine CN. This work will inspire the design of modified carbon nitride photocatalyst through precise modulation of structural defect and exotic element doping, and enhance the understanding on the correlation between catalyst structure and photocatalytic activity in H_2O_2 production.

The method used to examine the morphology of CN was scanning electron microscopy (SEM) imaging. The SEM image (Fig. 1b) shows that the CN has thick layers with agglomerated bulky structure. After modification, the SD-CN catalysts show folds and fractured morphology (Figs. 1c-e). This is because, during the heat treatment process, the sodium dicyandiamide eutectic salt breaks the carbon nitride structure, resulting a porous and fractured structure [31]. The results in Fig. S1 (Supporting information) show that the specific surface areas of CN and 10SD-CN are 4.29 m^2/g and 3.40 m^2/g, respectively, indicating that the high photocatalytic activity of the catalyst is not decisively related to its specific surface area.

As shown in Fig. 1f, the X-ray diffraction (XRD) patterns of CN displays two distinct diffraction peaks at 12.9° (100) and 27.1° (002), which are assigned to the in-plane structural packing of tri-*s*-triazine (heptazine) units and interlayer stacking of g-C_3N_4 sheets, respectively [36]. The (100) peak intensity decreases after the doping with sodium dicyandiamide, suggesting that Na atom can disrupt the ordered structure of the tri-*s*-triazine units and influence the reactivity of the dicyandiamide intermediates during the polymerization process. The intensity of the (002) peak is also reduced under high sodium dicyandiamide doping, suggesting a substantial disturbance of the lamellar structure of carbon nitride [37].

As shown in the FT-IR spectra (Fig. 1g), the stretching mode of the aromatic C–N heterocycle shows several peaks in both CN and SD-CN, which are situated between 1200 cm^{-1} and 1900 cm^{-1} [38]. Additionally, a new peak in SD-CN is found at 2180 cm^{-1}, which is associated with the -C≡N asymmetric stretching vibration. This implies that the cyano functional group is introduced into the CN structure during the doping and polymerization process with sodium dicyandiamide [35]. It is also noticed that the intensity of cyano group peak increases with the increasing sodium dicyandiamide content.

X-ray photoelectron spectroscopy (XPS) was then carried out to analyze the surface chemistry of the catalyst. The XPS survey spectra show (Fig. 1h) that the content of Na in the modified CN increases with the increasing doping of sodium dicyandiamide. As shown in Table S1 (Supporting information), the C/N atomic ratio of SD-CN gradually increased from 0.94 to 1.02 compared to that of pristine CN, which indicates the introduction of N vacancies. To further elucidate the type of N structures in SD-CN, the high resolution N 1s spectra were obtained (Fig. S2 in Supporting information). The peak at 398.6 eV is assigned to the sp^2 hybridized N atom in the aromatic ring plane (C–N=C, $N2_C$), while the 399.8 eV peak is due to the tertiary nitrogen atom in N-3C ($N3_C$). The -NH_x group is responsible for the peak at 401.0 eV, and π-π^* structure is found at 404.3 eV [39]. The contents of different N and C species are summarized in Table S2 and S3 (Supporting information). It shows that the content of $N3_C$ decreases with the increase of sodium dicyandiamide doping, which indicates a gradual increase of $N3_C$ vacancies. In contrast, there are three distinct peaks in the C 1s XPS spectra of 10SD-CN and 20SD-CN (Fig. S3 in Supporting information), which are located at 284.8 eV (C–C and C=C), 286.6 eV (C–NHx/C≡N), and 288.1 eV (N–C=N), respec-

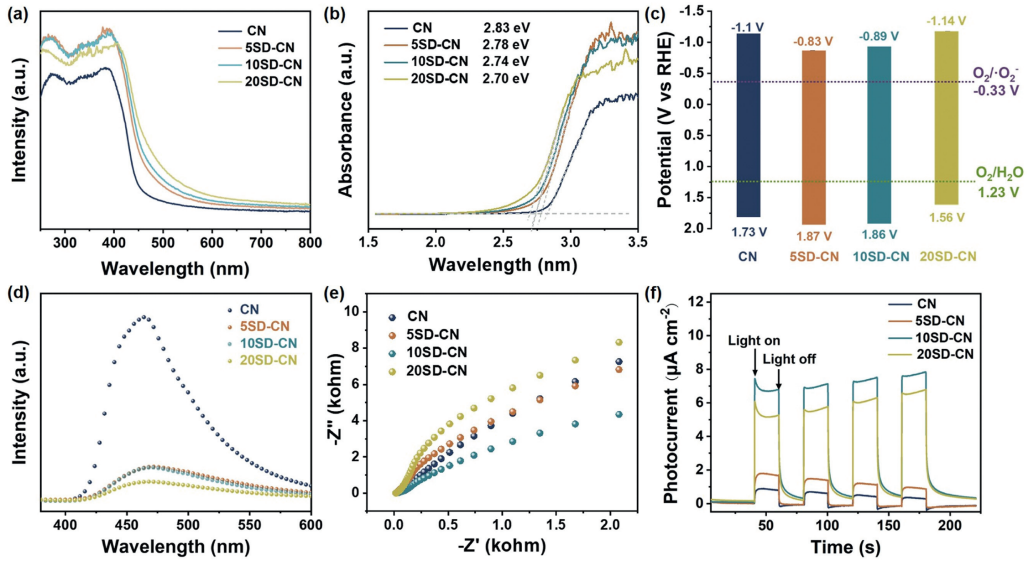

Fig. 2. (a) UV–vis–NIR spectra of CN, 5SD-CN, 10SD-CN, and 20SD-CN. (b) The energy gaps of CN, 5SD-CN, 10SD-CN, and 20SD-CN estimated by the Tauc plots. (c) The electronic band structure, (d) PL spectra, (e) EIS Nyquist plots and (f) transient photocurrent responses of CN, 5SD-CN, 10SD-CN, and 20SD-CN.

tively [40]. From the C 1s spectra, it is noticed that the peak at 286.6 eV (C–NHx/C≡N) gradually increases as the sodium dicyandiamide content is increased, which is consistent with the infrared spectroscopy results.

The TPD experiment was carried out to study the oxygen adsorption capacity of 10SD-CN. As shown in Fig. S4 (Supporting information), the oxygen adsorption on 10SD-CN is higher than that of the CN in the adsorption region (<350 °C), which indicates that 10SD-CN has a higher binding strength to O_2 than CN. The enhanced oxygen adsorption capacity of 10SD-CN can be ascribed to the cyano group [41]. The zeta potential analysis was used to analyze the surface charge status of the catalysts. As shown in Fig. S5 (Supporting information), CN reaches the point of zero charge (PZC) at pH 3.9. In contrast, the 10SD-CN sample is negatively charged in the pH range from 2 to 9. Therefore, under the photocatalytic reaction condition (pH 7), the 10SD-CN surface is more negatively charged, which makes it easier to react with H^+, and the negative charge also facilitates the adsorption of O_2, which can promote the subsequent photocatalytic H_2O_2 generation [42].

The electron spin resonance (ESR) spectroscopy can detect the unpaired electrons on the carbon atom of aromatic ring in carbon nitride. As shown in Fig. S6 (Supporting information), 10SD-CN exhibits a stronger signal than CN under dark condition, indicating that more unpaired electrons are present on the carbon atoms of 10SD-CN due to the nitrogen vacancies [43]. Upon visible light irradiation, 10SD-CN displays a stronger signal compared with that in dark, indicating a greater number of unpaired electrons which can promote photocatalytic reaction [44].

To investigate the effect of sodium dicyandiamide on the light absorption performance and energy band structure, UV–vis near infrared (UV–vis–NIR) spectroscopy was carried out for the prepared catalysts. As shown in Fig. 2a, all samples exhibit considerable light absorption. It is shown that a progressive red shift of the absorption edge can be observed after modification and doping, and SD-CN exhibits stronger absorption of visible light than CN [45]. Based on the above UV–vis diffuse reflectance spectra (DRS) results, the corresponding energy band gap (E_g) was calculated by the transformed Kubelka-Munk functional equation [46]. As shown in Fig. 2b, the band gap of CN, 5SD-CN, 10SD-CN, and 20SD-CN are 2.83, 2.78, 2.75, and 2.70 eV, respectively. The reduced band gaps indicates that the introduction of Na intercalation and N vacancies can reduce the band gap and improve the light trapping ability of carbon nitride [47].

To further explore the band position of the catalysts, XPS valence band (XPS-VB) was determined. The VB potentials of CN, 5SD-CN, 10SD-CN, and 20SD-CN samples were located at 2.29, 2.43, 2.42, and 2.18 eV, respectively (Fig. S7 (Supporting information)). In order to eliminate the measurement error of the contact potential difference (*vs.* NHE, pH 7) between the sample and the spectrometer, the actual VB position was calculated using Eq. 1, where Φ(3.88 eV) represents the function of electrical energy of XPS analyzer [48]. So, the actual VB positions calculated for CN, 5SD-CN, 10SD-CN, and 20SD-CN were 1.73 V, 1.87 V, 1.86 V, and 1.56 V, respectively. Mott-Schottky analysis (Fig. S8 in Supporting information) further reveals that the VB locations of CN, 5SD-CN, 10SD-CN, and 20SD-CN are 1.78 V, 1.94 V, 1.83 V, and 1.53 V (*vs.* RHE), respectively, which are similar to the VB positions determined by XPS results. The estimated band structures of CN and SCN5 are presented in Fig. 2c.

$$\text{EVB } (vs.\ \text{NHE}) = \Phi + \text{EVB}\left(\text{determined by XPS}\right) - 4.44 \quad (1)$$

The introduction of alkali metal and defects will affect the separation and complexation rates of photoexcited electrons and holes, and tune the energy band structure of CN, leading to enhanced charge carrier migration efficiency. The photoluminescence (PL) emission spectra were also obtained to investigate the recombination efficiency of photogenerated electron-hole pairs. Generally, lower PL intensity indicates higher charge separation rate. Based on the results (Fig. 2d), CN shows high intensity PL signals because of its inherent charge recombination. In contrast, the PL peak of SD-CNs is greatly decayed, indicating that the introduction of Na^+ and -C≡N can effectively inhibit the rate of electron-hole pairs recombination [49]. It has been reported that due to the weaker electronegativity of the carbon atom than that of the nitrogen atom, the -C≡N group is electronegative and can accept the electrons generated by photoexcitation, which facilitates the electron-hole pair separation and conversion [50]. Therefore, the introduction of -C≡N groups in CN will result in relatively longer lifetime of charge carriers.

Electrochemical impedance spectroscopy (EIS) is another useful method to evaluate the charge carrier separation and transfer properties. The EIS measurement results in Fig. 2e demonstrate that the interfacial electron transfer resistance decreases first un-

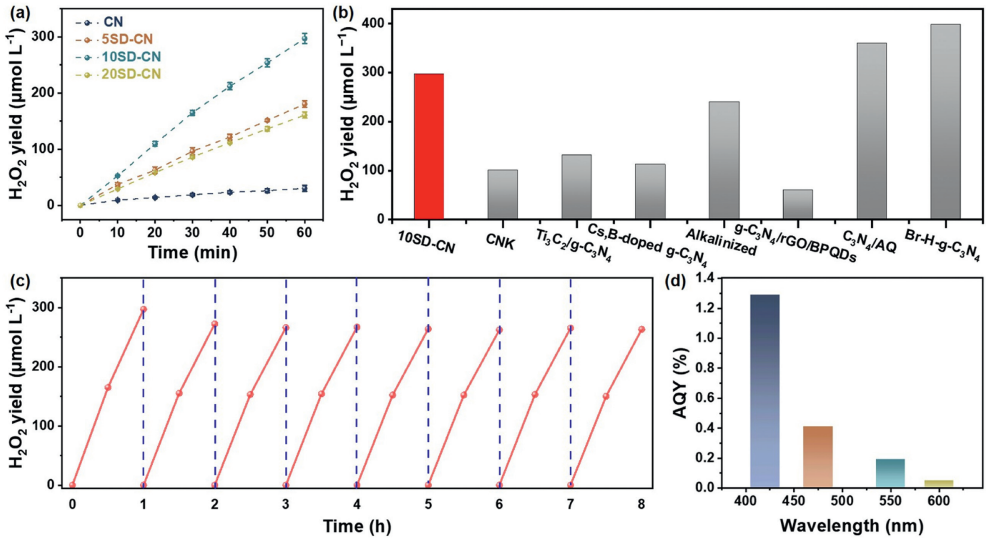

Fig. 3. (a) H_2O_2 production performance of CN, 5SD-CN, 10SD-CN, and 20SD-CN. Test condition: water (45 mL), IPA (5 mL), catalyst (10 mg), visible light irradiation ($\lambda \geq$ 420 nm). (b) The comparison of H_2O_2 production performance of 10SD-CN with other reported photocatalysts. Details of the catalyst comparison can be found in Table S7 (Supporting information). (c) Cycling test of photocatalytic H_2O_2 generation with 10SD-CN. (d) Apparent quantum yield (AQY) of 10SD-CN under different wavelength conditions.

der low doping/modification level (5SD-CN and 10SD-CN) and will increase under high doping/modification level (20SD-CN). This is caused by the combined effects of Na doping and structural defects, which are typically thought of as charge-binding sites [51]. However, too many defects will influence the capacity of the catalyst to transfer electrons on its surface. To learn more about the samples' charge separation and transfer kinetics, photocurrent measurements were carried out. As shown in Fig. 2f, the photoelectric current test shows that CN displays a weak photocurrent density of 0.67 μA/cm^2, while 10SD-CN shows the highest photocurrent density (7.09 μA/cm^2) among the catalysts. This further suggests that 10SD-CN exhibits higher charge-carrier migration efficiency and lower electron-hole pair complexation rate compared with those of CN, 5SD-CN, and 20SD-CN [52].

The photocatalytic hydrogen peroxide production efficiencies of CN and SD-CNs were then studied under visible light irradiation ($\lambda \geq$ 420 nm) condition. Fig. 3a shows that CN has a low H_2O_2 yield of 30.4 μmol L^{-1} h^{-1}, while the H_2O_2 yield of 5SD-CN increases to 180.5 μmol L^{-1} h^{-1}. The best photocatalytic performance is obtained with 10SD-CN (297.2 μmol L^{-1} h^{-1}), which is approximately 9.8 times that of CN. This H_2O_2 yield rate of 10SD-CN is very competitive among the CN-based H_2O_2 evolution catalysts (Table S7 in Supporting information and Fig. 3b), which can be attributed to the synergy of sodium doping and nitrogen defects. It is noticed that when the quantity of sodium dicyandiamide is too high, the photocatalytic hydrogen peroxide production yield decreases to 160.8 μmol L^{-1} h^{-1} (20SD-CN). This is because there is less electron transfer capacity at the catalyst interface as a result of excessive defects [53]. Moreover, several common electron donors including MeOH, EtOH, IPA were used as the sacrificial agent to study the effect of electron donor on the photocatalytic H_2O_2 evolution performance. The results in Fig. S9 (Supporting information) indicate that 10SD-CN with 10% IPA in the reaction solution exhibits higher H_2O_2 yield rate than the other electron donors. The formation (k_f) and decomposition (k_d) kinetics of H_2O_2 were calculated to further understand the activity of SD-CN catalysts. As shown in Fig. S10 and Table S4 (Supporting information), 10SD-CN shows the highest H_2O_2 formation rate of 5.897 μmol L^{-1} min^{-1}, and low H_2O_2 decomposition rate of 0.0059 min^{-1} compared with other tested catalysts, further confirming its outstanding H_2O_2 generation performance.

A useful photocatalyst needs to have high stability during the reaction process. As demonstrated in Fig. 3c, after 8 cycles (8 h) test, the 10SD-CN catalyst retains 90% activity in H_2O_2 generation. To study the stability of the sample after the reaction, the used 10SD-CN was characterized by SEM, XRD, FTIR, and XPS analysis. As shown in Fig. S11 and Table S5 (Supporting information), the fresh and used 10SD-CN show very similar structures and properties based on the characterization results, confirming the good stability of the polymer catalyst during the reaction. The above results indicate that the prepared 10SD-CN photocatalyst has excellent physicochemical stability and recyclability. The AQY of 10SD-CN was further calculated, and the AQY under monochromatic light irradiation at 420, 475, 550 and 600 nm were 1.29%, 0.41%, 0.19%, and 0.05%, respectively (Fig. 3d and Table S6 in Supporting information).

To reveal the behind mechanism of the enhanced photocatalytic performance and to better understand the process of photocatalytic H_2O_2 generation, some condition-controlled experiments were carried out. Fig. 4a illustrates the H_2O_2 production rate is severely suppressed to 123.4 μmol L^{-1} h^{-1} for 10SD-CN when Ar was continuously injected. Conversely, injecting oxygen increases the yield rate to 684.6 μmol L^{-1} h^{-1}, which is much higher than that of CN (81.2 μmol L^{-1} h^{-1}), suggesting that dissolved oxygen is the essential raw material for the synthesis of hydrogen peroxide [54]. Therefore, rather than water oxidation reaction (WOR) [55], it is suggested that oxygen reduction reaction (ORR) is the primary pathway for the formation of H_2O_2. A series of studies have demonstrated that the ORR pathway can be categorized into two-step single electron reaction (Eqs. 2 and 3 and a direct one-step two-electron reaction Eq. 4) [56,57]:

$$O_2 + e^- \rightarrow {}^{\bullet}O_2^- \quad (2)$$

$$O_2^- + 2H^+ + e^- \rightarrow H_2O_2 \quad (3)$$

$$O_2 + 2e^- + 2H^+ \rightarrow H_2O_2 \quad (4)$$

To determine the ORR pathway, *p*-benzoquinone (*p*-BQ) was added as an $^{\bullet}O_2^-$ inhibitor, and the experimental results showed that H_2O_2 production was greatly inhibited, suggesting that $^{\bullet}O_2^-$ plays an important role in participating the H_2O_2 production (Fig. 4b) [58]. To study if the presence of *p*-BQ influences the iodometry test result, we tested two H_2O_2 sample solutions (one

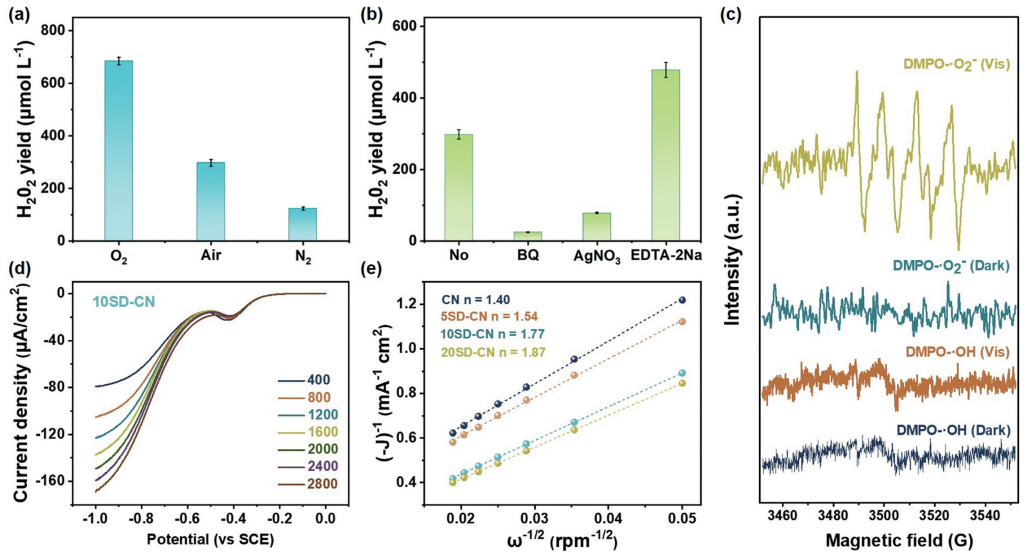

Fig. 4. Photocatalytic H_2O_2 production under different (a) atmosphere and (b) solution conditions with 10SD-CN. Condition: water (45 mL), isopropanol (5 mL), catalyst (10 mg), visible light irradiation ($\lambda \geq 420$ nm). (c) ESR spectra of DMPO-·O_2^- and DMPO-·OH with 10SD-CN under visible light irradiation. (d) LSV curves of 10SD-CN measured on RDE at different rotating speeds. Condition: 0.1 mol/L Na_2SO_4 solution (pH 6.6), scan rate of 5 mV/s. (e) Koutecky-Levich plots obtained from the RDE results.

with *p*-BQ). According to Fig. S12 (Supporting information), the iodometry test yielded the same H_2O_2 concentrations in the solutions with and without *p*-BQ, indicating that the influence of *p*-BQ was negligible. In addition, we employed $AgNO_3$ and EDTA-2Na as the scavengers of electron (e^-) and hole (h^+), respectively, in the control experiment [59]. The H_2O_2 production rate dropped sharply when $AgNO_3$ was introduced to the photocatalytic reaction system (Fig. 4b), demonstrating the critical role of photogenerated electrons in ORR. In contrast, it is shown that the yield of H_2O_2 increases when EDTA-2Na is added, which is because the capture of holes can facilitate the transfer of electrons during the photocatalytic process.

The electron spin resonance (ESR) spectra were obtained to study the intermediates (·O_2^- and ·OH) generated during the photocatalytic process. As shown in Fig. 4c, no ·OH signal is observed under light irradiation, confirming that ·OH is not generated in the photocatalytic reaction and the water oxidation reaction does not produce H_2O_2. However, a strong signal of ·O_2^- is observed under light irradiation, which indicates that ·O_2^- is the main radical involving the photocatalytic reaction [60]. As previously discussed, the electron transfer number in the ORR process is critical for H_2O_2 production; therefore, a rotating disk electrode (RDE) was used to characterize the average electron transfer number (*n*) [61]. Fig. 4d and Fig. S13 (Supporting information) show the LSV curves of catalysts at different rotating speeds. According to Koutecky-Levich calculation, the values of *n* for CN, 5SD-CN, 10SD-CN, and 20SD-CN were calculated as 1.40, 1.54, 1.77, and 1.87, respectively (Fig. 4e). These results suggest that one-electron and two-electron oxygen reduction occurs simultaneously during the reaction [62]. The increase of the n value suggests that the catalyst prefers the two-electron transfer pathway in H_2O_2-generated reaction. This is because the nitrogen vacancy sites in the modified carbon nitride are more selective for the two-electron transfer pathway [63]. Based on the above analysis, a reaction pathway for H_2O_2 production with 10SD-CN is proposed. First, O_2 is adsorbed onto the C sites around the $N3_C$ vacancies. Then, after absorbing light energy, the catalyst produces electron-hole pairs. Due to the synergistic interaction between alkali metal doping and defects, the catalyst exhibits a high charge separation ability and can effectively reduce O_2 to ·O_2^-. Eventually, ·O_2^- gains another electron and reacts with H^+ in solution to form H_2O_2.

In conclusion, we successfully synthesize modified carbon nitrides with abundant active sites by thermal polymerization using sodium dicyandiamide as a modifier. The modified carbon nitrides are applied for photocatalytic synthesis of H_2O_2. The introduction of sodium element improves the light absorption ability, while the nitrogen defects provide more active sites and promote the charge separation during the photocatalytic process. Due to the synergistic effect of alkali metal doping and nitrogen defects, the 10SD-CN catalyst achieves a hydrogen peroxide yield of 297.2 μmol L^{-1} h^{-1} under visible light irradiation. This work provides new insights in constructing novel and efficient non-homogeneous photocatalyst for solar energy driven synthesis of H_2O_2. Currently, the primary obstacles of photocatalytic H_2O_2 production by C_3N_4-based catalysts in actual water environments include weak anti-interference, low stability, low visible light absorption, problematic catalyst recovery, *etc*. Depending on the application scenario, stable and highly efficient photocatalysts must be developed for the applications in real water environment. To enable the recovery of the catalyst, it is necessary to develop more effective immobilization methods and design more practical reaction devices.

Declaration of competing interest

The authors declare that they have no known competing financial interests or personal relationships that could have appeared to influence the work reported in this paper.

Acknowledgments

This work was supported by the National Natural Science Foundation of China (No. 22376159) and the Fundamental Research Funds for the Central Universities (No. 2022–4-ZD-08).

Supplementary materials

Supplementary material associated with this article can be found, in the online version, at doi:10.1016/j.cclet.2024.109886.

References

[1] J.K. Edwards, B. Solsona, E. Ntainjua, et al., Science 323 (2009) 1037–1041.
[2] Z. Lu, G. Chen, S. Siahrostami, et al., Nat. Catal. 1 (2018) 156–162.

[3] H. Su, C. Christodoulatos, B. Smolinski, et al., Engineering 5 (2019) 849–854.
[4] B. Shao, L. Shen, Z. Liu, et al., Chem. Eng. J. 455 (2023) 140476.
[5] W. Fan, B. Zhang, X. Wang, et al., Energy Environ. Sci. 13 (2020) 238–245.
[6] Z. Chen, D. Yao, C. Chu, S. Mao, Chem. Eng. J. 451 (2023) 138489.
[7] Y. Pan, Z. Peng, Z. Liu, et al., J. Environ. Chem. Eng. 10 (2022) 107366.
[8] X. Zhang, S. Tong, D. Huang, et al., Coord. Chem. Rev. 448 (2021) 129067.
[9] F. Qin, E. Almatrafi, C. Zhang, et al., Angew. Chem. Int. Ed. 62 (2023) e202300256.
[10] C. Xia, Y. Xia, P. Zhu, L. Fan, H. Wang, Science 366 (2019) 226–231.
[11] Y. Sun, L. Han, P. Strasser, Chem. Soc. Rev. 49 (2020) 6605–6631.
[12] J. Ma, X. Peng, Z. Zhou, Y. Shen, Y. Zhang, Chin. Chem. Lett. 34 (2023) 108784.
[13] C. Chu, Q. Li, W. Miao, et al., Appl. Catal. B: Environ. 314 (2022) 121485.
[14] T. Li, Y. Pan, B. Shao, et al., Adv. Funct. Mater. 33 (2023) 2304990.
[15] B. Shao, Z. Liu, L. Tang, et al., J. Hazard. Mater. 435 (2022) 129067.
[16] X. Wang, K. Maeda, A. Thomas, et al., Nat. Mater. 8 (2008) 76–80.
[17] B. Shao, Y. Xu, Z. Liu, et al., J. Clean Prod. 384 (2023) 135518.
[18] T. Wu, Q. He, Z. Liu, et al., J. Hazard. Mater. 424 (2022) 127177.
[19] Y. Shiraishi, Y. Kofuji, H. Sakamoto, et al., ACS Catal. 5 (2015) 3058–3066.
[20] X. Qian, Y. Wu, M. Kan, et al., Appl. Catal. B: Environ. 237 (2018) 513–520.
[21] L. Wu, S. An, Y.F. Song, Engineering 7 (2021) 94–102.
[22] Z. Yang, B. Guo, Z. Hu, et al., Chin. Chem. Lett. 35 (2024) 109251.
[23] Y. Wu, H. Che, B. Liu, Y. Ao, Small Struct. 4 (2023) 2200371.
[24] Y. Yang, Z. Zeng, G. Zeng, et al., Appl. Catal. B: Environ. 258 (2019) 117956.
[25] H. Ou, P. Yang, L. Lin, M. Anpo, X. Wang, Angew. Chem. Int. Ed. 56 (2017) 10905–10910.
[26] W. Wang, X. Li, F. Deng, et al., Chin. Chem. Lett. 33 (2022) 5200–5207.
[27] Y. Duan, Y. Wang, L. Gan, et al., Adv. Energy Mater. 11 (2021) 202004001.
[28] C. Feng, L. Tang, Y. Deng, et al., Adv. Funct. Mater. 30 (2020) 2001922.
[29] Q. He, C. Zhao, L. Tang, et al., Chemosphere 326 (2023) 138326.
[30] Z. Liu, M. He, L. Tang, et al., J. Colloid Interface Sci. 634 (2023) 255–267.
[31] S. Wu, H. Yu, S. Chen, X. Quan, ACS Catal. 10 (2020) 14380–14389.
[32] L. Zhou, J.Y. Lei, F.C. Wang, et al., Appl. Catal. B: Environ. 288 (2021) 119993.
[33] T. Wu, Z. Liu, B. Shao, et al., Chem. Eng. J. 447 (2022) 137332.
[34] C.C. Nguyen, T.O. Do, ACS Appl. Energ. Mater. 1 (2018) 4716–4723.
[35] Y. Pan, X. Liu, W. Zhang, et al., Chem. Eng. J. 427 (2022) 132032.
[36] D. Zhao, C.L. Dong, B. Wang, et al., Adv. Mater. 31 (2019) 1903545.
[37] H. Yu, R. Shi, Y. Zhao, et al., Adv. Mater. 29 (2017) 1605148.
[38] F. Dong, Z. Wang, Y. Sun, W.K. Ho, H. Zhang, J. Colloid Interface Sci. 401 (2013) 70–79.
[39] H. Zhang, L. Jia, P. Wu, et al., Appl. Surf. Sci. 527 (2020) 146584.
[40] F. Yang, D. Liu, Y. Li, L. Cheng, J. Ye, Appl. Catal. B: Environ. 240 (2019) 64–71.
[41] Y.X. Ye, C. Wen, J. Pan, et al., Appl. Catal. B: Environ. 285 (2021) 119726.
[42] G.h. Moon, M. Fujitsuka, S. Kim, et al., ACS Catal. 7 (2017) 2886–2895.
[43] M. Shen, L. Zhang, M. Wang, et al., J. Mater. Chem. A 7 (2019) 1556–1563.
[44] J. Li, Z. Zhang, W. Cui, et al., ACS Catal. 8 (2018) 8376–8385.
[45] B. Shao, X. Liu, Z. Liu, et al., Chem. Eng. J. 368 (2019) 730–745.
[46] H. Che, X. Gao, J. Chen, et al., Angew. Chem. Int. Ed. 60 (2021) 25546–25550.
[47] J. Tian, T. Wu, D. Wang, et al., Catal. Today 330 (2019) 171–178.
[48] Q. Dong, Y. Fang, Y. Shao, et al., Science 347 (2015) 967–970.
[49] T. Xiong, W. Cen, Y. Zhang, F. Dong, ACS Catal. 6 (2016) 2462–2472.
[50] G. Liu, G. Zhao, W. Zhou, et al., Adv. Funct. Mater. 26 (2016) 6822–6829.
[51] T. Yao, X. An, H. Han, J.Q. Chen, C. Li, Adv. Energy Mater. 8 (2018) 1800210.
[52] B. Shao, Z. Liu, G. Zeng, et al., Appl. Catal. B: Environ. 286 (2021) 119867.
[53] X. Wu, H. Ma, W. Zhong, J. Fan, H. Yu, Appl. Catal. B: Environ. 271 (2020) 118899.
[54] W. Miao, D. Yao, C. Chu, et al., Appl. Catal. B: Environ. 332 (2023) 122770.
[55] J. Xu, Q. Zhang, X. Gao, et al., Angew. Chem. Int. Ed. 62 (2023) e202307018.
[56] C. Chu, W. Miao, Q. Li, et al., Chem. Eng. J. 428 (2022) 132531.
[57] T. Wu, Q. Liang, L. Tang, et al., J. Hazard. Mater. 443 (2023) 130251.
[58] Y. Wang, D. Meng, X. Zhao, Appl. Catal. B: Environ. 273 (2020) 119064.
[59] T. Hou, H. Peng, Y. Xin, et al., ACS Catal. 10 (2020) 5502–5510.
[60] C.C. Chu, D.C. Yao, Z. Chen, et al., Small 19 (2023) 2303796.
[61] D. Yao, W. Miao, C. Chu, et al., Chem. Eng. J. 467 (2023) 143550.
[62] Y. Zhao, Y. Liu, Z. Wang, et al., Appl. Catal. B: Environ. 289 (2021) 120035.
[63] Y. Xie, Y. Li, Z. Huang, et al., Appl. Catal. B: Environ. 265 (2020) 118581.